

Characterization of spontaneous imbibition dynamics in irregular channels by mesoscopic modeling

Jiangtao Zheng^{a,b}, Zhiqiang Chen^b, Chiyu Xie^b, Ziyan Wang^b, Zhengdong Lei^c, Yang Ju^{a,d}, Moran Wang^{b,*}

^aState Key Laboratory of Coal Resources and Safe Mining, China University of Mining & Technology at Beijing, Beijing 100083, China

^bDepartment of Engineering Mechanics, School of Aerospace, Tsinghua University, Beijing 100084, China

^cResearch Institute of Petroleum Exploration & Development, Beijing 100083, China

^dState Key Laboratory for Geomechanics and Deep Underground Engineering, China University of Mining & Technology, Xuzhou 221006, China

ARTICLE INFO

Article history:

Received 17 May 2017

Revised 19 January 2018

Accepted 23 January 2018

Available online 31 January 2018

Keywords:

Spontaneous imbibition

Capillary pressure

Two phase flow

Irregular channel

Lattice Boltzmann method

ABSTRACT

Accurate knowledge of spontaneous imbibition in irregular channels is fundamentally important for a better understanding of the transport in a porous media. During the spontaneous imbibition, the wetting fluid is driven by the capillary pressure and retarded by the viscous drag, both of which are highly influenced by the channel geometry. As a result, accurate simulation of the process in complex geometries becomes important. In this study, an improved fluid-solid interaction force in the two-phase pseudopotential lattice Boltzmann method is proposed for the accuracy and stability in simulating the spontaneous imbibition behavior. After validation the simulated results against the theoretical results in a 2D straight channel, the method is employed to simulate the spontaneous imbibition in irregular channel models, which include a sine-shape channel, a wedge-shape channel and bifurcated channels. The results quantitatively revealed the influence of tortuosity, channel shape on the imbibition behavior and the competing interfaces advancing behavior in bifurcated channels.

© 2018 Elsevier Ltd. All rights reserved.

1. Introduction

Spontaneous imbibition happens ubiquitously in nature and daily life which become more predominant at small scales. An alternative term “capillary rise” is used for describing the same process in regular geometry models such as straight channels and cylindrical tubes [1]. In nature, the nepenthes take advantage of spontaneous imbibition to keep the rim of its pitcher wet for capturing insects [2]. Some shorebirds with long thin beaks, such as phalaropes, are evolved to rely on the surface tension of water to feed and drink [3]. Besides, numerous activities in daily life are related with spontaneous imbibition, for example, clean up spilt liquid with a towel, print ink on a paper, to name just a few. Spontaneous imbibition is also closely related to several practical applications, such as increasing oil recovering [4], the reason for low flow back rate after hydraulic fracturing in a shale gas reservoir [5], development of “lab on a chip” and related micro- and nanofluidic devices [6]. A deeper understanding of the physics behind spontaneous imbibition and the ability to predict the capillary flow be-

havior in porous media are crucial for numerous engineering applications.

The classical equation for describing the spontaneous imbibition dynamics is the Lucas-Washburn (LW) equation, which states that the meniscus advancing in a simple square-root-time (\sqrt{t}) manner. In general, the spontaneous imbibition is driven by an almost time-independent capillary pressure and retarded by an increasing viscous drag. Assuming a Hagen–Poiseuille flow driven by the constant capillary pressure but increasing viscous force, one can easily recover the LW equation [7]. Although the LW equation is derived based on the capillary flows in cylindrical tubes, this simple \sqrt{t} manner has shown its validity for describing the spontaneous imbibition in homogeneous porous structures [7,8] and even for nanoscale pores [9]. For example, Handy [10] developed a spontaneous imbibition law for conventional reservoir rocks which states the imbibed mass is proportional to \sqrt{t} . O’ Loughlin [11] investigate the capillary rise in glass capillaries and pointed out that the experimental results of pure glycerol perfectly agreed with the LW equation. Dimitrov et al. [12] studied the capillary rise in nanotubes by molecular dynamics method and indicate that the LW equation is applicable. Gruener et al. [7] studied the imbibition of water into Vycor glass, which contains nanoscale porous structures, and the experimental results showed that the LW equation

* Corresponding author.

E-mail address: mrwang@tsinghua.edu.cn (M. Wang).

is still valid. Several modified relationships for describing spontaneous imbibition in homogeneous porous media were developed by assuming the flow path as a bundle of independent capillaries. For example, Cai and Yu [13] took into account the influence of tortuosity of the porous structure by fractal theory and made a modification of the LW equation. Cai et al [14] developed a generalized equation of spontaneous imbibition which included the influence of channel tortuosity and cross-sectional shape. In general, the imbibition front propagates uniformly in homogeneous porous media and the LW equation is robust for describing the process.

However, for the spontaneous imbibition in long channels with axial variation [15] and heterogeneous porous media [16], theoretical derivation and experimental results showed some deviation from the LW equation. For instance, Reyssat et al. [15] demonstrated that the imbibition in a long wedge-shape channel gradually deviated from the \sqrt{t} manner. Imbibition in unconventional reservoir rocks, such as shale, is more complicated due to its complex porous structures and heterogeneous mineral composition [5]. Experimental studies showed that the time exponent deviated from 0.5 for some shale reservoir samples [17–19]. Several attempts were made to provide a reasonable explanation. For example, Hu et al. [18,19] argued that the low connectivity of the porous structure in shale caused the time exponent less than 0.5. Liu et al. [20] reviewed the spontaneous imbibition data of shale and claimed that the non-Darcy flow in low-permeability shale was responsible for the deviation. There are still disputations in describing the imbibition dynamics in the complex porous material [11]. In order to gain insight into the imbibition mechanisms, it is better to start from the pore scale and get a direct observation of the imbibition process [21]. A deeper understanding of the physics behind spontaneous imbibition and the ability to predict the flow behavior in complex porous media are of paramount importance to the practical applications mentioned above.

With the rapid development of detection equipment and computer reconstruction methods, characterization of the porous structure in a material at different scale is now accessible. For example, an integrated focused ion beam and high-resolution scanning electron microscopy method (FIB-SEM) [22] was employed to obtain the nano-scale porous structure in shale. As a non-destructive method, X-ray computed tomography (CT) [23] was used to access the 3D porous structure of a material, but with a lower resolution than FIB-SEM. Besides above mentioned experimental observation method, the numerical reconstruction methods provide an effective and economical way to reproduce the pore structures. Some representative reconstruction methods include the process based method [24], statistical information based method [25,26] and random generation-growth algorithm termed as quartet structure generation set (QSGS) [27,28]. The porous structures reproduced by these experimental and reconstruction methods provide the basis for studying the imbibition process numerically, which can improve the understanding of complex multi-phase flow in a porous media.

With the availability of digital porous structure, direct simulation of the imbibition process at pore scale become possible. However, accurate simulation of the two-phase flow in a porous structure faces great challenges due to the inherent complexity of the flow behavior, which include moving interface with complex topology and interface break-up and coalescence [29]. For a macroscopic approach, interfaces are either explicitly tracked (sharp interface method) or implicitly handled (diffusive interface method). The later one is more convenient for simulating the two-phase flow in complex porous structures [30]. Alternatively, the pore network model (PNM) was employed to simulate the imbibition process but with too much simplification of the porous structure [31,32]. Another possible approach to study the imbibition phenomenon is the molecular dynamics (MD) [12]. However, this method is usu-

ally employed in nano-scale and very small time interval, which becomes too computationally demanding to be applied at larger scales. The lattice Boltzmann method (LBM), which is a mesoscopic method and based on the discretization of Boltzmann kinetic equation, shed light on the modeling of complex fluid flows [33]. With the improvements on achieving high density ratio [34,35], easily adjusting viscosities and surface tension [36,37] and calculation efficiency [30], the LBM has shown its ability in simulating the two-phase flow phenomena in complex porous structures [36,38–45]. Some representative LBM multiphase models include the color gradient LBM [30,46,47], pseudopotential or SC-LBM [48,49], free-energy LBM [50,51] and mean-field LBM [52]. Several critical review papers and books can be found in [53–56]. The understanding of complex two-phase flow in porous media was greatly improved with the development of these simulation methods.

Among the LBM simulation methods, the SC-LBM has been widely applied to investigate the multi-phase flows due to its conceptual simplicity and computational efficiency [54]. The SC-LBM represents the interaction force at mesoscopic scale using a pseudopotential which depends on the local density [48,49]. When the interaction strength factor below a critical value, the separation of the two phases happens automatically with a diffusive interface formed between. Moreover, a non-zero surface tension exists in the system. In addition, properly including the adhesive force between fluid nodes and solid nodes permits the simulation of spontaneous imbibition. For example, Raiskinmäki et al. [57] employed the SC-LBM to study the capillary rise in a cylindrical tube and pointed out a reasonable result could be obtained when the tube diameter in the simulation is characterized by at least 30 lattices. Diotallevi et al. [58,59] studied the capillary rise in a straight channel and argued the high grid resolution limitation could be alleviated when a higher density ratio (about 30) between the two phases was used. More recently, the SC-LBM was employed by Son et al. [60] to investigate the capillary flow in polygonal tubes with special consideration of the influence of pore corners. As listed above, most of the existing SC-LBM for studying the spontaneous imbibition is limited to simple geometries. There are several possible reasons responsible for this. First, the need of high grid resolution restricts the calculation of imbibition in complex porous structures due to a massive computational demand [59]. Second, the implementation of fluid-solid interaction usually leads to an unphysical fluid density accumulation near the wall, especially for the case of spontaneous imbibition in porous structure [61]. A versatile SC-LBM is needed, which is reliable for uncovering the spontaneous imbibition behavior in complex geometries.

In this work, an improved SC-LBM is proposed which enables the accurate spontaneous imbibition simulation. Specifically, a new fluid-solid interaction force is incorporated in the model which has a better control of fluid density accumulation near the wall. The influence of channel geometry on imbibition is then investigated and the applicability of LW is discussed. The remainder of the paper is structured as follows: in Section 2 the basic concept of SC-LBM and the newly proposed implementation of fluid-solid interaction force are introduced. The validation of the proposed method is presented in Section 3. The spontaneous imbibition in irregular channels is studied in Section 4. Some useful discussions are presented in Section 5. We make concluding remarks in Section 6.

2. Methods

2.1. Single-component two-phase SC-LBM

A single-component, two-phase SC-LBM was employed for simulating the imbibition process. The LBM is a mesoscopic method which considers the fluid motion by a set of particle distribution function [53]. The single-component lattice Boltzmann equation

with the Bhatnagar–Gross–Krook (BGK) [62] collision operator is written as:

$$f_\alpha(\mathbf{x} + \mathbf{e}_\alpha \Delta t, t + \Delta t) - f_\alpha(\mathbf{x}, t) = \frac{\Delta t}{\tau} [f_\alpha(\mathbf{x}, t) - f_\alpha^{\text{eq}}(\mathbf{x}, t)] + \mathbf{F}_\alpha \Delta t \quad (1)$$

where $f_\alpha(\mathbf{x}, t)$ is the density distribution function in α direction, $f_\alpha^{\text{eq}}(\mathbf{x}, t)$ is the equilibrium density distribution function, \mathbf{F} representing the forcing term whose role will be discussed later in the framework of inter-particle interactions, τ is the relaxation time which is related to the kinetic viscosity of the fluid as $\nu = \frac{c^2}{3}(\tau - 0.5\Delta t)$ [63]. In this work, τ is set equal to 1. $c = \Delta x/\Delta t$ is the lattice speed with Δx and Δt as the lattice spacing and time step respectively, both of which equal to 1 in the lattice system. The directional velocity \mathbf{e}_α is defined as follows for D2Q9 model [64]:

$$\mathbf{e}_\alpha = c \begin{bmatrix} 0 & 1 & 0 & -1 & 0 & 1 & -1 & -1 & 1 \\ 0 & 0 & 1 & 0 & -1 & 1 & 1 & -1 & -1 \end{bmatrix} \quad (2)$$

The equilibrium density distribution function is defined as:

$$f_\alpha^{\text{eq}}(\mathbf{x}, t) = w_\alpha \rho(\mathbf{x}, t) \times \left[1 + 3 \frac{\mathbf{e}_\alpha \cdot \mathbf{u}^{\text{eq}}}{c^2} + 4.5 \frac{(\mathbf{e}_\alpha \cdot \mathbf{u}^{\text{eq}})^2}{c^2} - 1.5 \frac{(\mathbf{u}^{\text{eq}})^2}{c^2} \right] \quad (3)$$

For D2Q9 model, $w_\alpha = 4/9$ ($\alpha = 0$), $w_\alpha = 1/9$ ($\alpha = 1, 2, 3, 4$), $w_\alpha = 1/36$ ($\alpha = 5, 6, 7, 8$). ρ is fluid density which is calculated by $\rho = \sum_\alpha f_\alpha$. The shifted equilibrium velocity represented by \mathbf{u}^{eq} , is calculated by:

$$\mathbf{u}^{\text{eq}} = \frac{\sum_\alpha f_\alpha \mathbf{e}_\alpha}{\rho} + \frac{\tau \mathbf{F}}{\rho} \quad (4)$$

The SC-LBM is based on the idea of representing intermolecular interactions at the mesoscopic scale via a density-dependent nearest-neighbor pseudopotential. The interaction forces, which includes fluid–fluid interaction force (i.e. cohesive force or internal force, \mathbf{F}_{int}) and fluid–solid interaction force (i.e. adhesive force, \mathbf{F}_{ads}), is defined as $\mathbf{F} = \mathbf{F}_{\text{int}} + \mathbf{F}_{\text{ads}}$. The cohesive force and adhesive force are usually calculated by the following equations:

$$\mathbf{F}_{\text{int}}(\mathbf{x}, t) = -G\psi(\mathbf{x}, t) \sum_\alpha w_\alpha \psi(\mathbf{x} + \mathbf{e}_\alpha \Delta t, t) \mathbf{e}_\alpha \quad (5)$$

$$\mathbf{F}_{\text{ads}}(\mathbf{x}, t) = -G\psi(\mathbf{x}, t) \sum_\alpha w_\alpha \psi(\rho_w) s(\mathbf{x} + \mathbf{e}_\alpha \Delta t, t) \mathbf{e}_\alpha \quad (6)$$

where ψ is the pseudopotential function which is related to local density. G is the interaction strength parameter, with a negative value leading to an attractive force. As mentioned before, the separation of the two phases is permitted when G is less than a critical value. From hereafter, the phase with larger density is referred as liquid phase (ρ_l) and the phase with smaller density is referred as gas phase (ρ_g). The adhesive force between a fluid node and surrounding solid nodes is generally calculated by Eq. (6), in which a fictitious density is defined on the solid node as ρ_w . Usually, ρ_w is set as a constant in previous studies. A new method for defining ρ_w is proposed in this work, which will be described in detail in the next section. $s(\mathbf{x} + \mathbf{e}_\alpha \Delta t, t)$ is an index function, which equals to 1 for a solid node and 0 for a fluid node. A bounce-back boundary condition is applied on all solid nodes to maintain a non-slip velocity condition of fluids on solid walls [65]. The pseudopotential function employed in this work is the same as proposed by Shan and Chen in 1993 [48], which takes the form as:

$$\psi(\rho) = \rho_0 \left[1 - \exp\left(-\frac{\rho}{\rho_0}\right) \right] \quad (7)$$

where the reference density ρ_0 is set equal to 1.

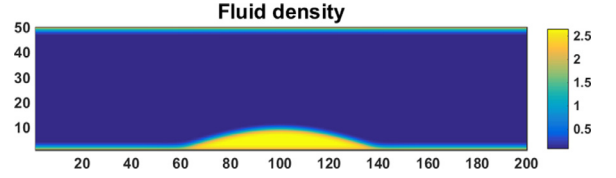


Fig. 1. Unphysical density accumulation near the wall.

2.2. Fluid–solid interaction force

The fluid–solid interaction force determines the wettability of the wall. As reviewed by Chen et al. [53], there are generally two methods to implement the adhesion force and obtain different contact angles. The first one is keeping the $\psi(\rho_w)$ in Eq. (6) equal to 1 and changing the value of G to get different contact angles [60]. The second approach is set different values of ρ_w to obtain desirable contact angles [66]. However, both methods suffered from unphysical density accumulation near the wall (about 5 lattices) even for a static contact angle calculation, as shown in Fig. 1.

The reason is that a uniformly high attractive force is applied near all the solid nodes. This leads to the density accumulation near the solid nodes even for the region away from the liquid droplet, as shown in Fig. 1. In order to have a better control over the density distribution near the wall, a new fluid–solid interaction force is introduced as follows:

$$\mathbf{F}_{\text{ads}}(\mathbf{x}, t) = -G\psi(\mathbf{x}, t) \sum_\alpha w_\alpha \psi(\beta \bar{\rho}_f) s(\mathbf{x} + \mathbf{e}_\alpha \Delta t, t) \mathbf{e}_\alpha \quad (8)$$

The difference between Eq. (8) and Eq. (6) is that the fictitious wall density, i.e. $\beta \bar{\rho}_f$, is a variable in the calculation rather than a constant value. The value of $\bar{\rho}_f$ on a solid node in a 2D case is calculated by averaging the surrounding fluid density in its 8 neighboring nodes. The value of β is a strength factor which controls the wettability of the wall. The value of β is equal to 1 when $\bar{\rho}_f < 2\rho_g$ and equal to the setting value when $\bar{\rho}_f \geq 2\rho_g$. Under this setting, the high interaction force between solid nodes and gas nodes is inhibited. It should be noted that the above method is similar to the modified ψ based method proposed by Li et al. [67] and De Maio et al. [61]. These methods incorporate the fluid–solid interaction by an analog to the fluid–fluid interaction and consider the fictitious wall density or index function as a variable rather than a constant.

3. Validations

When employing SC-LBM for a complex flow simulation, the macroscopic parameters, i.e. coexist density, surface tension and contact angle, are usually determined through simple settings of simulations [48,49,66]. In this part, these parameters, which are essential for the spontaneous imbibition simulation, are determined first. Then the capillary rise in a straight 2D channel is simulated and compared with the analytical solution for validation purpose.

3.1. Coexistence density and surface tension

In the coexistence density and surface tension calculations, only the fluid–fluid interaction is involved. With the value of interaction strength G being set, the coexistence density ρ_l and ρ_g and the surface tension are determined. The value of G is set equal to -6 in this work for simulation accuracy of spontaneous imbibition [59].

In the coexistence density calculation, a random density value was defined throughout a fully periodic computational domain of $N_x \times N_y = 50 \times 100$ lattices [56,59]. The densities in the upper part nodes and lower part nodes were set slightly above and below the

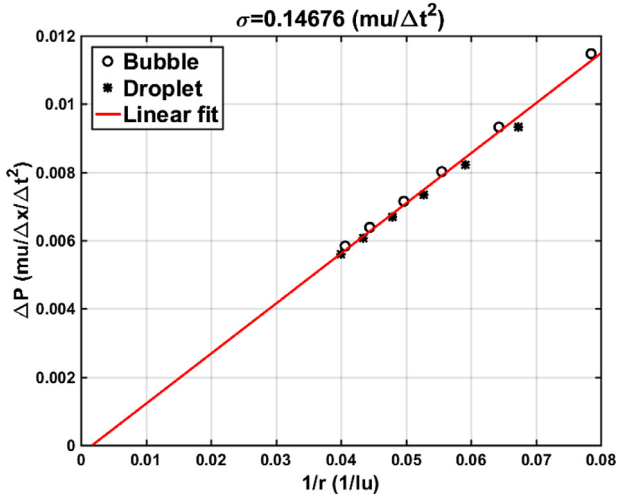


Fig. 2. Pressure difference (ΔP) inside and outside the bubble or droplet as a function of the reciprocal of the final radius ($1/r$). A linear fit is plotted as a red line on the figure. (For interpretation of the references to colour in this figure legend, the reader is referred to the web version of this article.)

critical value of $\ln(2)$, respectively. With the evolution of the calculation, a flat interface between the liquid phase and gas phase was gradually formed. The equilibrium ρ_l and ρ_g equal to 2.649 and 0.0735, respectively.

In the surface tension calculation, the pressure difference is calculated of a droplet (bubble) surrounded by gas (liquid) bulk in a fully periodic domain. A series of bubbles (gas phase) and droplets (liquid phase) with radiuses of 15, 17, 19, 21, 23, 25 lattices respectively were initialized in a fully periodic computational domain of $N_x \times N_y = 101 \times 101$ lattices. The final bubble or droplet sizes and the pressure differences were recorded. This type of calculation also served as a validation of SC-LBM by investigating whether the Laplace equation was recovered. According to Laplace equation, the pressure difference (ΔP) between liquid and gas phase in a 2D case is calculated by:

$$\Delta P = \frac{\sigma}{r} \quad (9)$$

where σ is the surface tension and r is final radius of the bubble or droplet after 100,000 iteration steps. The rim of the final bubble or droplet was defined as the position with the mean density, i.e. $(\rho_l + \rho_g)/2$. The ΔP was calculated by the pressure difference 10 lattices inward and outward of the rim. The pressure on each node of the simulated results was calculated by [66]:

$$P(\mathbf{x}, t) = \frac{c^2}{3}\rho + \frac{c^2}{6}G\psi^2(\mathbf{x}) \quad (10)$$

The calculated results of ΔP and $1/r$ were plotted in Fig. 2. As shown, a linear relationship exists between ΔP and $1/r$. The fitted line almost across the zero point, which agreed with the Laplace equation. The calculated result of surface tension with $G = -6$ was about 0.147 in lattice unit.

3.2. Static contact angle

The static contact angles of a liquid droplet on a flat surface with different values of β were calculated by incorporating the proposed fluid-solid interaction. Specifically, the adhesive force generated by the fluid-solid interaction was calculated according to Eq. (8). In the calculation, a domain of $N_x \times N_y = 201 \times 50$ lattices was adopted with top and bottom layers set as solid walls and periodic boundary set on the left and right ends. Initially, a semi-circular droplet was placed on the bottom wall through the following

equation [68,69]:

$$\rho(x, y) = \frac{\rho_l + \rho_g}{2} - \frac{\rho_l - \rho_g}{2} \tanh \left[\frac{2(R - R_0)}{W} \right] \quad (11)$$

where W is the initial interface thickness, which is chosen as 5 lattices and $R = \sqrt{(x - N_x/2)^2 + y^2}$. The radius of the initial semi-circular droplet R_0 is equal to 20 lattices.

In the calculation, the fictitious wall density distribution was determined before calculating the pseudopotential ψ at each time step. A large range of static contact angle can be achieved with different values of β . The calculated static contact angle results after 100,000 time steps for six different β values are shown in Fig. 3. As shown, the unphysical density accumulation of the wetting phase near the wall was eliminated. The interface is again defined at the position with the mean density, which is denoted as a red line on Fig. 3. The contact angle $\theta \in [0, \pi]$ was calculated by [64]:

$$\theta = \arctan \frac{b}{2(r - h)} \quad (12)$$

where b and h are the base length and height of the droplet on each figure respectively. The radius of the droplet (r) is calculated by $r = (4h^2 + b^2)/8h$.

3.3. Capillary rise in a 2D straight channel

The proposed method was employed to simulate the capillary rise in a 2D straight channel for validation purpose. The driving force was the capillary force and the resistance force was the viscous force. Starting from the balance between total momentum changes in the channel and the force acting on the liquid and gas system, one may get the following equation for describing the capillary rise in a 2D straight channel:

$$\frac{2\sigma \cos(\theta)}{H} - \frac{12(dl/dt)}{H^2} [\mu_g(L - l) + \mu_l l] = 0 \quad (13)$$

where the first and second part in the left-hand side of the equation represent the capillary pressure and viscous pressure respectively. Reorganizing the equation, we have:

$$\frac{dl}{dt} = \frac{H\sigma \cos(\theta)}{6[\mu_g(L - l) + \mu_l l]} \quad (14)$$

where H and L are the width and length of the channel respectively, l is the capillary rise length of the liquid phase, μ_g and μ_l are the viscosity of gas phase and liquid phase respectively. Several simulation results of the capillary rise by SC-LBM have already been published in the literature and acceptable results were obtained when the grid resolution was sufficiently high. For instance, Diotallevi et al. [59] represented the 2D channel width by 121 lattices to reproduce accurate capillary rise results. In the simulation of capillary rise in cylindrical tube, Raiskinmäki et al. [57] pointed out the tube diameter should be represented by at least 30 lattices to obtain an accurate result.

The following simulation results demonstrated that good simulation results can be obtained even for low grid resolution by applying the proposed fluid-solid interaction scheme. Fig. 4(a) illustrates the initial setup for the capillary rise simulation with a computational domain of $N_x \times N_y = 1000 \times 12$ and channel width and length equal to 10 and 500, respectively. Other simulations in following parts also employ the similar initial setup with the channels placed on the right half of the computational domain. The liquid plug of 500 lattice length has 10 lattices overlap with the walls. Periodic boundary condition was imposed on all boundaries except the channel walls boundaries. Four capillary rise cases with β values equal to 2.80, 2.32, 1.84 and 1.36 respectively were simulated

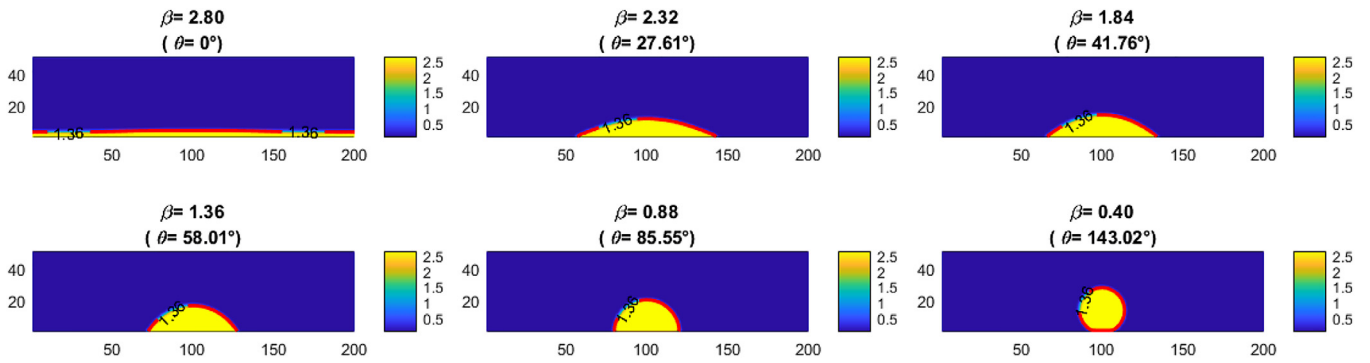


Fig. 3. Static contact angles with different values of β . A red line is denoted on each figure which represents the interface between liquid and gas phase. (For interpretation of the references to colour in this figure legend, the reader is referred to the web version of this article.)

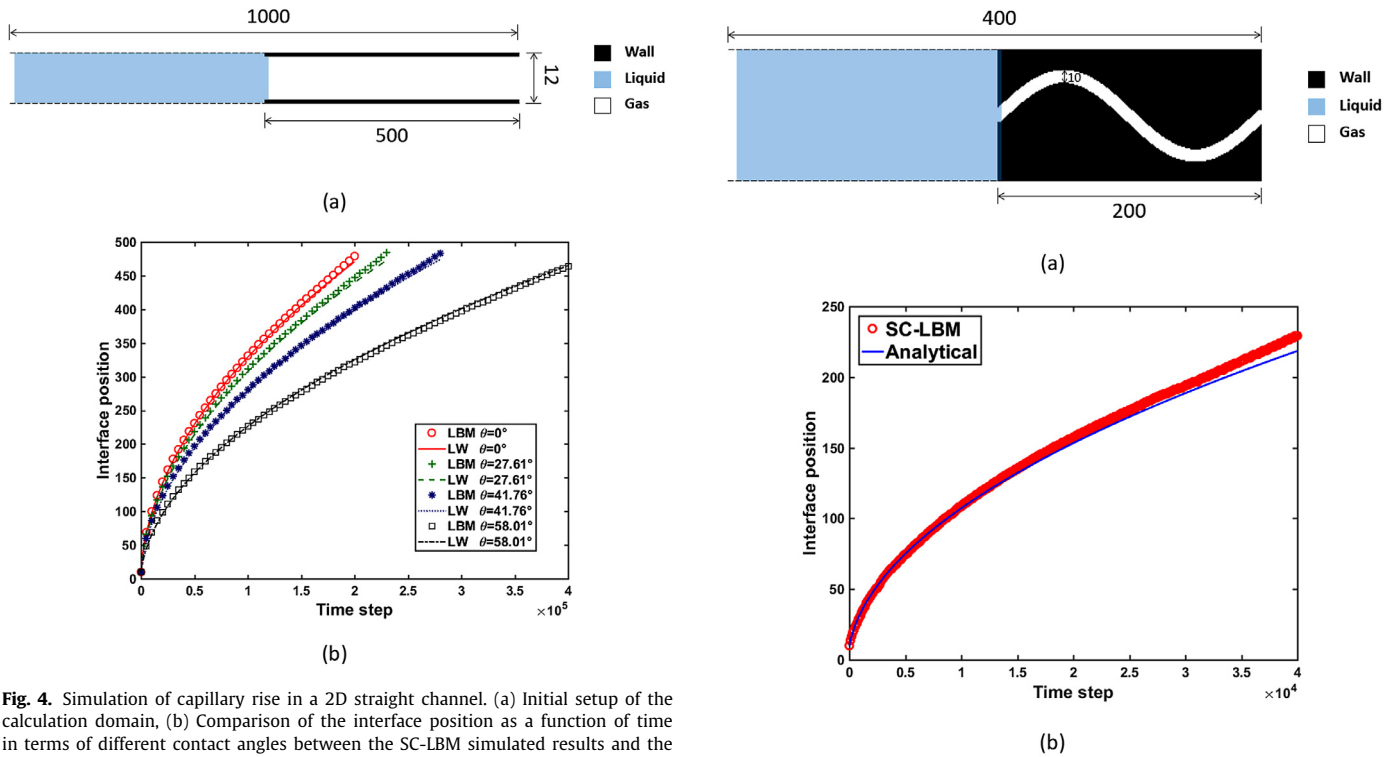


Fig. 4. Simulation of capillary rise in a 2D straight channel. (a) Initial setup of the calculation domain, (b) Comparison of the interface position as a function of time in terms of different contact angles between the SC-LBM simulated results and the analytical solutions.

to check whether the method validates for different contact angle cases.

Comparisons of the simulated results and the analytical results of Eq. (14) were plotted in Fig. 4(b) which show good agreements. By employing the proposed method for the fluid-solid interaction, accurate results were permitted even for the channel width of 10 lattices. This is particularly important for the simulation of imbibition in the complex porous structure by SC-LBM when considering the computational efficiency.

4. Spontaneous imbibition in irregular channels

4.1. Spontaneous imbibition in a sine-shape channel

The spontaneous imbibition in a sine-shape channel was simulated with the proposed method in the first place. The initial setup for the simulation was shown in Fig. 5(a) with a computational domain of $N_x \times N_y = 400 \times 100$. The channel width was 10 lattices. In the simulation, the β value was set equal to 2.80 to simulate a

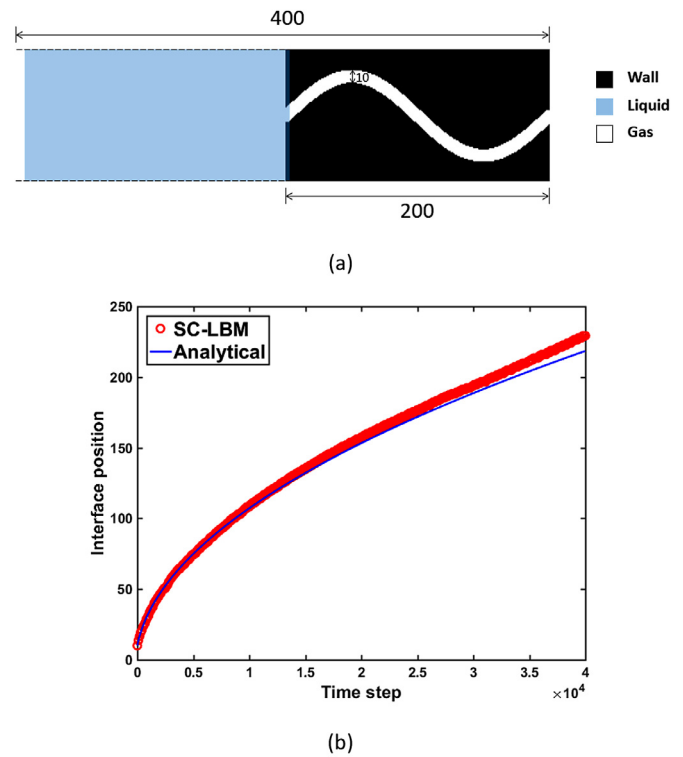


Fig. 5. Simulation of spontaneous imbibition in a 2D sine-shape channel. (a) Initial setup of the calculation domain, (b) Comparison of the interface position as a function of time between the SC-LBM simulated results and the analytical solutions.

complete wetting case and all other parameters were set the same with straight channel case.

Comparisons of the simulated results and the analytical results of Eq. (14) are plotted in Fig. 5(b) which show a good agreement. This demonstrates that the LW equation is validated for a tortuous channel with constant channel width.

4.2. Spontaneous imbibition in a 2D wedge-shape channel

In this part, the imbibition dynamics in a 2D wedge-shape channel was simulated by the SC-LBM and compared with the analytical results [15]. The model used in the simulation is shown in Fig. 6(a). The inlet width of the wedge equal to 10 lattices and the outlet width equal to 50 lattices. The length of wedge equals to 200 lattices. A critical length (L_c) was defined, after which, the time exponent gradually changed from 1/2 to 1/3 [15]. For the ge-

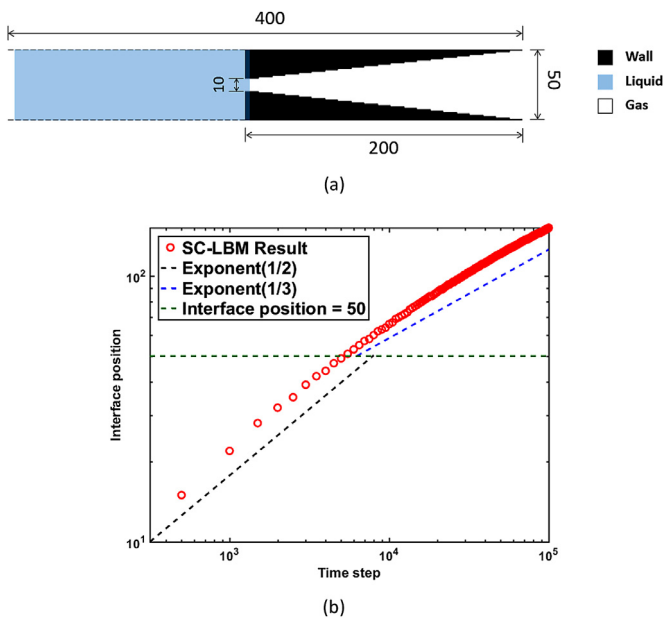


Fig. 6. Simulation of spontaneous imbibition in a 2D wedge-shape channel. (a) illustration of the model, (b) front interface position as a function of time.

ometry defined in Fig. 6(a), the critical length (L_c) equal to 50 lattices.

Fig. 6(b) showed the front interface position as a function of time in a double logarithmic coordinate. The critical length and power functions with time exponent equal to 1/2 and 1/3 respectively were also plotted. As compared, the simulated results correctly reproduced the imbibition trend in 2D wedge-shape channel. Before the interface reached the critical position, it generally followed the \sqrt{t} manner. After that, the exponent of the power law asymptotically equal to 1/3. The simulation results agreed with the analytical results which further demonstrated the feasibility of the proposed method in studying the imbibition process.

4.3. Spontaneous imbibition in bifurcated channels

The imbibition process in bifurcated channels was investigated which was primarily important for a better understanding of the spontaneous imbibition in complex porous structures. A similar process was also investigated by Wolf et al. [70] using a lattice-gas automata model based on field mediators. In our work, the “skeleton” of bifurcated channels was first drawn in a domain of $N_x \times N_y = 200 \times 100$. As shown in Fig. 7(a), the “skeleton” of small and big bifurcations were represented by red and blue solid line with lengths of 211 and 178 pixels, respectively. The inlet and outlet channels with lengths of 22 pixels are connected with the two bifurcated channels at points “C1” and “C2” and represented by black solid lines. Then the geometrical models used for the simula-

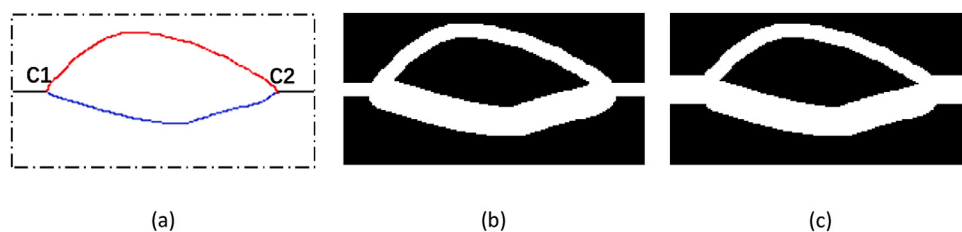


Fig. 7. Construction of the bifurcated channel models with the effective width of the small bifurcation equal to 10 pixels and that of the big bifurcation equal to 20 pixels. (a) the skeleton of the channels, (b) model A, with small inlet and outlet channels, (c) model B, with big inlet and outlet channels. (For interpretation of the references to colour in this figure legend, the reader is referred to the web version of this article.)

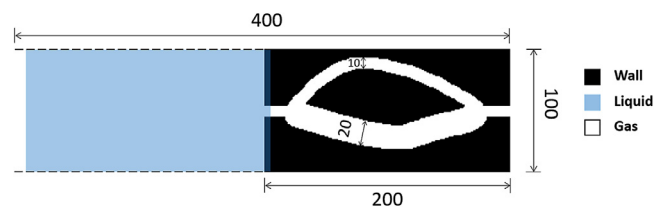


Fig. 8. Model used for the SC-LBM simulation.

tion were constructed. Each pixel on the skeleton was set as a circle center for creating the channels. The circle radii used for generating the small and big bifurcations were 5 pixels and 10 pixels respectively. Two models (A and B) were constructed with the only difference in the inlet and outlet channel width. For the model A, the inlet and outlet channel have widths the same as the small bifurcation, as shown in Fig. 7(b). For the model B, the inlet and outlet channel have widths the same as the big bifurcation, as shown in Fig. 7(c). The model generation method can be considered as a reverse process of skeleton extraction of porous media introduced by Silin et al. [71].

The imbibition processes in the two models were investigated for a deeper understanding of the spontaneous imbibition dynamics. One distinct feature of the bifurcated model is that the small and big bifurcations connected with each other at the inlet and outlet. In other words, these two bifurcations are not independent. For independent capillaries, i.e. channels directly touch with a liquid reservoir, the meniscus velocity is larger in the channel with larger width, as described in Eq. (14).

However, the imbibition dynamics in the bifurcated models are quite different. The spontaneous imbibition process in model A and model B were simulated by the proposed method, as shown in Fig. 8. Snapshots of the spontaneous imbibition processes in the two models were shown in Fig. 9 and Fig. 10, respectively. For the case of model A (as shown in Fig. 9), the meniscus in the small bifurcation reached the point C2 first and waited for the meniscus in the big bifurcation. In contrast, the meniscus in the big bifurcation reached the point C2 first for the case of model B (as shown in Fig. 10). When the meniscus in one of the bifurcation reached the point C2, it seemed paused because the “effective width” ahead was large enough and the capillary pressure was nearly zero. The positions of menisci in the two bifurcations were plotted as a function of time in Fig. 11(a) and (b) for the two models, respectively. It should be noted that the only difference between the two models is the widths of the inlet and outlet channels. However, the imbibition behavior after meniscus split was very different and the propagation of the meniscus to the outlet for the model A took about three times as long as the case of model B. In general, the menisci propagation in the two bifurcations first compete with each other and then wait for the other after the quicker one reached the point C2.

Special concerns of the imbibition dynamics were given at a time range when the meniscus split happened at the point C1.

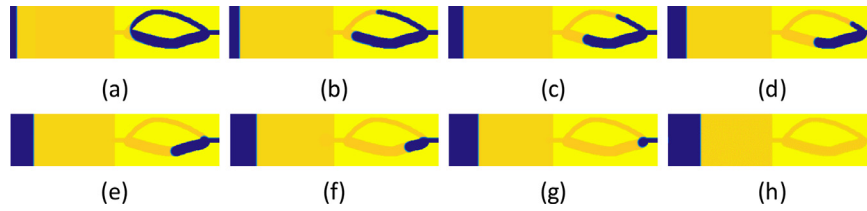


Fig. 9. Snapshot of the imbibition process in the model A. (a)–(f) imbibition at time step 10,000–80,000. The interval of the snapshots is 10,000 time steps.

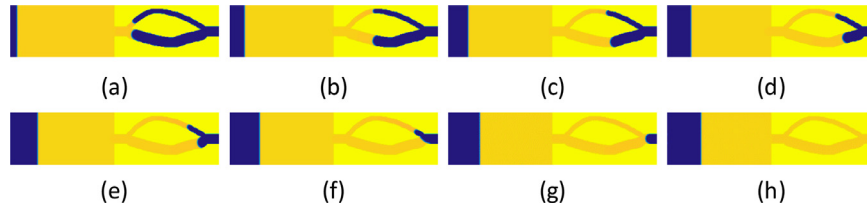


Fig. 10. Snapshot of the imbibition process in the model B. (a)–(f) imbibition at time step 2000–30,000. The interval of the snapshots is 4000 time steps.

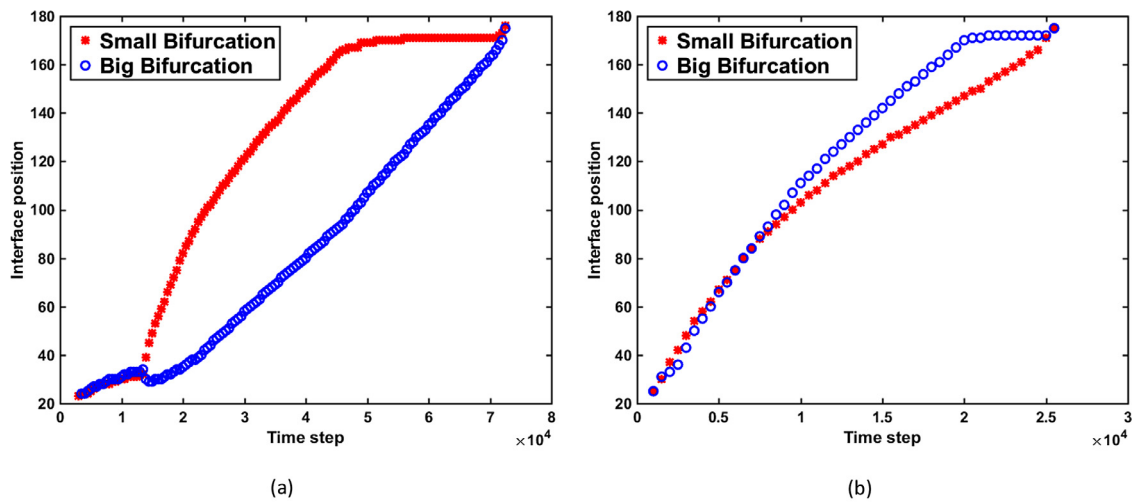


Fig. 11. Front interface position as a function of time in the bifurcated channel models. (a) the case of model A, (b) the case of model B.

The meniscus, as a whole, gradually moved forward before the split. Thus, at the time when the meniscus touched the point C1, the menisci velocities in the two bifurcations should be the same. However, the force balance in the system was broken due to a sudden increase of the capillary forces. The capillary pressure in the small bifurcation was larger than that in the big bifurcation and both of them larger than the capillary pressure before the meniscus split. Meanwhile, the resistance force, which was still dominantly induced by the inlet channel, should be almost the same. With this analysis, the meniscus in the big bifurcation will be arrested and even moving backward at a time range just after the meniscus splits, which can be observed in the Fig. 11. Meanwhile, the meniscus velocity in the small bifurcation showed a sudden increase.

The velocity fields around point C1 were shown in Figs. 12 and 13 for the two models, respectively. As shown, most of the velocity vectors were firstly towards the point C1 and then quickly changed to the direction of the small bifurcation for both models. Moreover, the meniscus propagation in the big bifurcation was retarded and even moving backward due to the larger capillary force in the small bifurcation and the insufficient supply from the inlet channel. This phenomenon was more predominant for the model A. A significantly high initial meniscus velocity in the small bifurcation was formed in the model A. This partially explained that the meniscus in the small bifurcation reached its end first for the

model A. Due to a relatively larger inlet channel width in model B, the retardation effect in the big bifurcation was not as remarkable as the case of model A. Although the initial velocity in the small bifurcation was also larger and the meniscus in the big bifurcation was retarded for a while, the interface in the big bifurcation reached its end first due to a smaller viscous retarding effect.

In addition, the pressure and velocity evolution were extracted throughout the whole process for a better understanding of the spontaneous imbibition behavior in the bifurcated models. Due to the diffusive meniscus calculated by the SC-LBM has a width about 5 lattices, the capillary pressures (P_c) in the bifurcations were defined as the pressure difference at 5 lattices ahead and behind the interfaces. The pressure difference (ΔP) between the point 5 lattices behind the interface and the start point of a bifurcation was recorded. In addition, ΔP between the end point and start point of the inlet channel was also recorded. Fig. 14(a) and (b) plotted these pressures of the two models, respectively. The velocity in the inlet channel was defined as the average velocity in the middle cross-section of the inlet channel. The velocity in a bifurcation was defined as the average velocity at the position 5 lattices behind the interface. Fig. 15(a) and (b) plotted these velocities of the two models, respectively.

In a spontaneous imbibition process, P_c can be considered as the driving force (positive value in the Fig. 14(a) and (b)). On the other hand, ΔP can be considered as the resisting force (negative

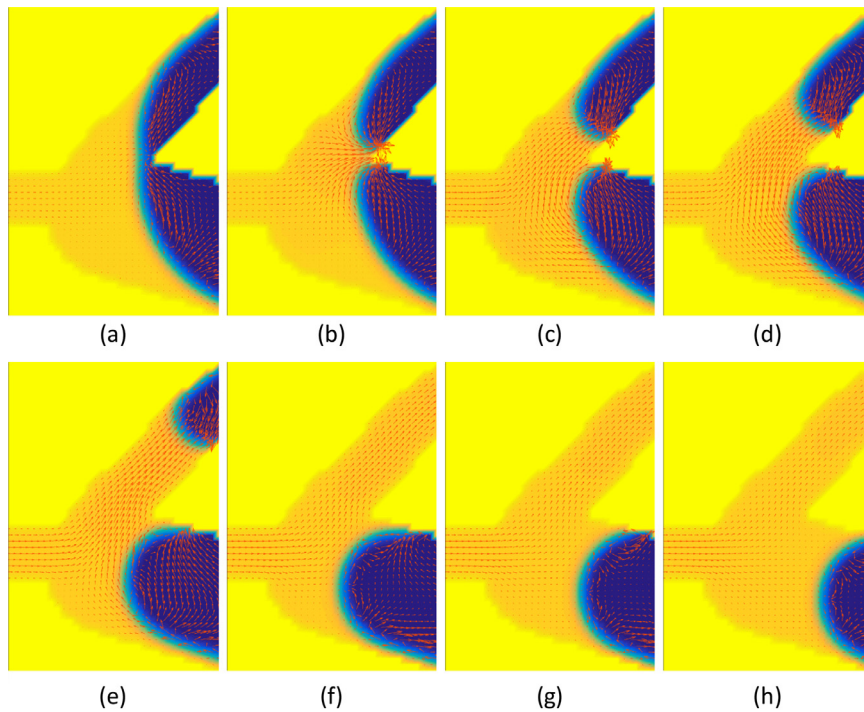


Fig. 12. Snapshot of the velocity field in the model A. (a)-(h) Velocity field at time steps equal to 13,550, 13,600, 13,650, 13,700, 14,000, 15,600, 18,500 and 21,000 respectively.

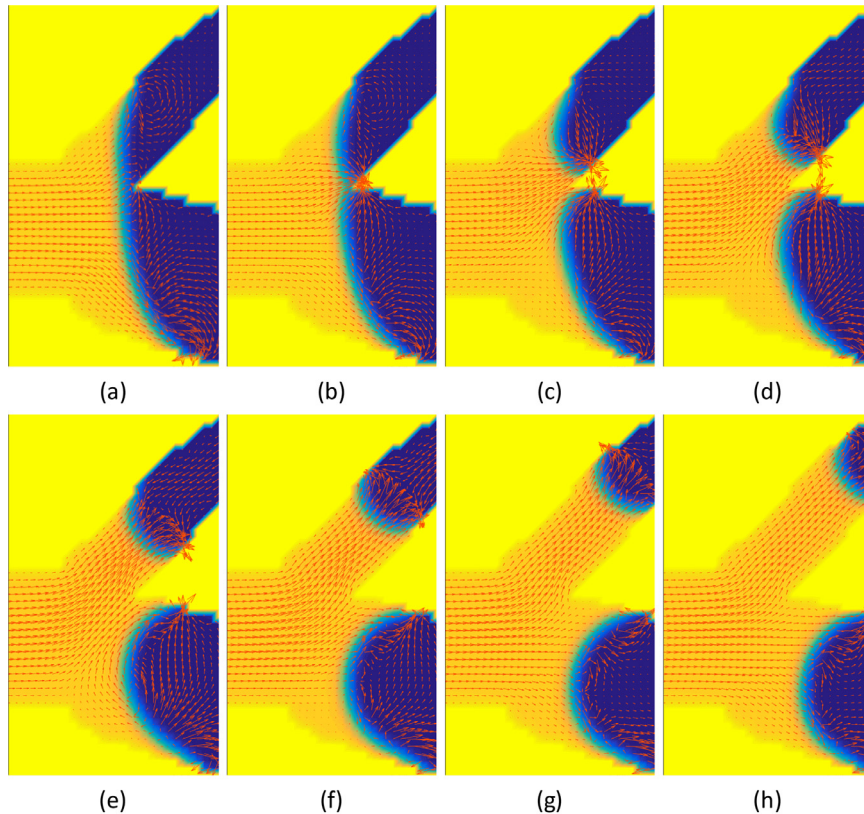


Fig. 13. Snapshot of the velocity field in the model A. (a)-(h) Velocity field at time steps equal to 1670, 1700, 1730, 1760, 1850, 2000, 2200 and 2400 respectively.

values in the Fig. 14(a) and (b)). As shown, for both models the capillary pressure in the small bifurcation was larger than that in the big bifurcation in a time range after the meniscus split. Meanwhile, the resistance force in the small bifurcation was also larger than that in the big bifurcation. The resistance force provided by

the inlet channel for model A was larger than that in the model B due to its smaller width. The meniscus split at time step 13,600 for model A and at time step 1760 for model B. When the meniscus split, the driving forces rapidly increased for both models. This led to an overall flux jump as shown in the velocity curve of the

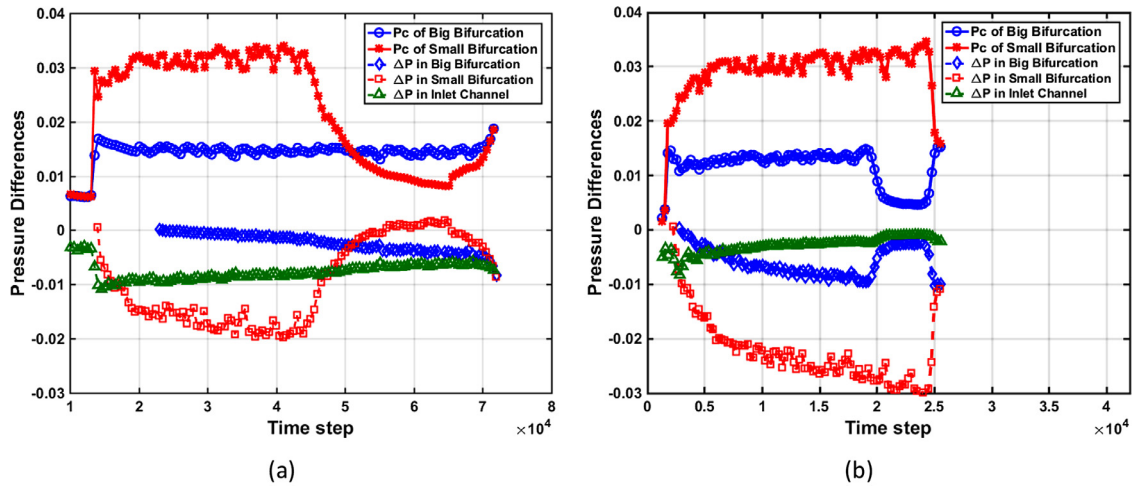


Fig. 14. Capillary pressures and pressure differences along with the meniscus propagation. (a) the case of model A, (b) the case of model B.

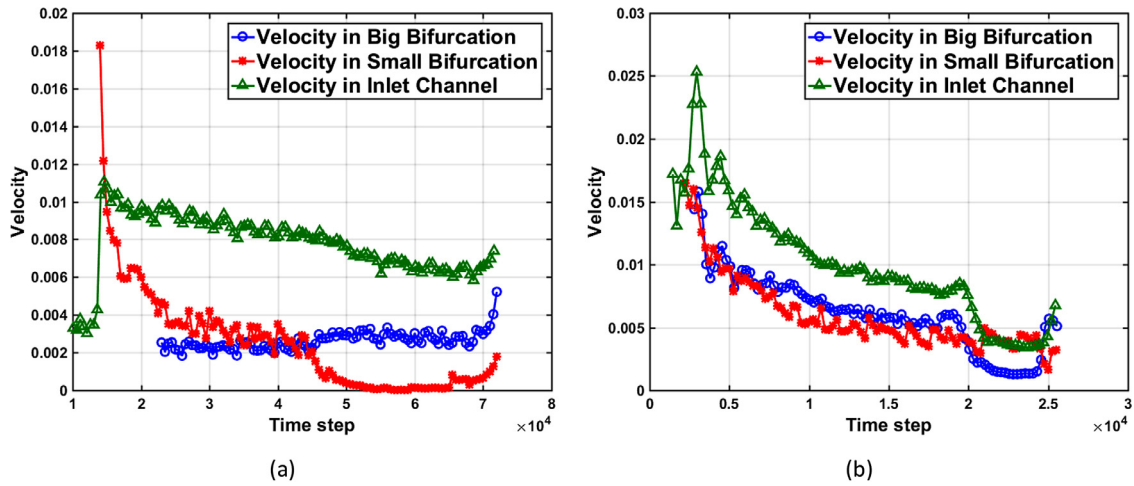


Fig. 15. Velocity dynamics in the two bifurcations and the inlet channel along with the meniscus propagation. (a) the case of model A, (b) the case of model B.

inlet channel in Fig. 15(a) and (b), which followed by a rapid resistance force increase in the inlet channel. Along with the meniscus propagation in the bifurcations, the resistance force provided by the inlet channel gradually decrease because of the velocity in the system decrease.

As mentioned above, the width of the inlet channel significantly influenced the imbibition in the bifurcations. For the model A, the inlet channel width is equal to the width of the small bifurcation. The velocity in the small bifurcation is even larger than that in the inlet channel just after meniscus split, as shown in Fig. 15(a). This is possible considering that the interface in the big bifurcation moving backward and served as an additional supply for the propagation in the small bifurcation. Beyond this severe transient period of the meniscus split in the model A, the velocity in the small bifurcation gradually decreased and the velocity in the big bifurcation nearly kept a constant and increased after the interface in the small bifurcation reached its end. For model B, the velocities in the inlet channel and two bifurcations gradually decrease. The meniscus velocity in big bifurcation was generally larger than that in the small bifurcation and reached the point C2 first. After the meniscus in the big bifurcation reached its end, the velocity in the inlet channel experienced a quick decrease and the velocity in the small bifurcation showed a slight increase.

Throughout the above analysis, it is found that the inlet channel width has a decisive effect on the imbibition behavior in the

bifurcations. After the meniscus split, the velocity in the small bifurcation was larger and the meniscus propagation in the two bifurcations competed with each other. The meniscus propagation in one bifurcation was enhanced when the other reached the bifurcation end.

5. Discussion

Previous work has documented the effectiveness of using SC-LBM to investigate the spontaneous imbibition dynamics in simple geometries, such as straight channels [58,59], cylindrical tubes [57] and polygonal cross-section tubes [60]. However, the accuracy and/or the efficiency of employing the method to probe the spontaneous imbibition dynamics in irregular channels were limited. The reasons, to the best of our knowledge, were related with the unphysical fluid density condensation near the wall. In this study, a modified method for incorporating the fluid-solid interaction force was proposed, which enable accurate imbibition results obtained with fewer coarser resolution. A series of spontaneous imbibition process in a variety of irregular channel models was investigated by the proposed method. Although seemed simple, these irregular channel models may serve as basic components of a porous structure. In specific, the results observed in the simple bifurcated channel models can be used for a better understanding of the imbibition pattern in a complex porous structure.

However, some limitations are worth noting. Firstly, despite its success in simulating multi-phase flows, the SC-LBM has drawn much criticism due to the spurious velocity produced near curved surfaces. This spurious velocity mainly arises from insufficient isotropy of the discrete gradient operator [72,73]. Although certain improvements were achieved [73], incorporating such modification made the implementation of wall boundaries more complex. A high spurious velocity near the intersection area between menisci and solid walls can be observed in our simulation. However, the velocity profile several lattices away from the interface obeys a classical parabolic profile. More importantly, good agreements between the simulation results and the analytical results can be achieved for capillary rise cases in terms of different contact angle, as shown in Fig. 4. It seems that the spurious velocity observed in several interface nodes have a limited influence on the overall imbibition process. Secondly, only capillary force and viscous force were involved and a classical Stokes flow was assumed in the calculation. Other forces, such as gravity force and external forces, should be taken into consideration for a real engineering application. Moreover, a velocity slip phenomenon at the walls should be investigated at a nano-scale [12]. In addition, the simulations in this study focused on 2D cases, although the extension to 3D cases was straightforward. Future works therefore include studying the cases in the 3D complex structures and involving other possible mechanisms, which would be helpful to gain a deeper understanding of the spontaneous imbibition behavior in real engineering applications.

6. Conclusions

A modified SC-LBM proposed in this work was shown to be able to accurately simulate the spontaneous imbibition in irregular channels. By incorporating the fluid-solid interaction force with the newly defined fictitious wall density, the unphysical fluid density condensation near the wall was eliminated and capillary rise dynamics in a 2D straight channel of only 10 lattices wide was precisely reproduced. The proposed method was then employed to simulate the imbibition in a sine-shape channel, a 2D wedge-shape and bifurcated channels. The result of the sine-shape channel demonstrated the spontaneous imbibition in a tortuous channel with constant width is similar to that in a straight channel. In the 2D wedge-shape channel case, the relationship between front interface position and time gradually deviated from the \sqrt{t} manner after the front interface passed over a critical length. The simulation results of imbibition in the bifurcated channel models showed competitive menisci advancing phenomena after the meniscus split. The width of the inlet channel has a great influence on the subsequent menisci propagation in the bifurcations. In summary, the proposed method can accurately recover the spontaneous imbibition process in irregular channels and may provide a possible approach to be used in real engineering applications.

Acknowledgments

The authors are grateful to the National Key R & D Program of China(2016YFC0600705), National Major Project for Science and Technology of China(2017ZX05003-006), National Natural Science Foundation of China (Grant No. U1562217, 51674251, 51727807), China Postdoctoral Science Foundation (Grant No. 2017M610877), and National Science and Technology Major Project on Oil and Gas(No.2017ZX05013001) for the financial support.

Reference

[1] Ishakoglu A, Baytas AF. The influence of contact angle on capillary pressure-saturation relations in a porous medium including various liquids. *Int J Eng Sci* 2005;43:744–55.

[2] Chen H, Zhang P, Zhang L, Liu H, Jiang Y, Zhang D, et al. Continuous directional water transport on the peristome surface of *Nepenthes alata*. *Nature* 2016;532:85–9.

[3] Prakash M, Quéré D, Bush JW. Surface tension transport of prey by feeding shorebirds: the capillary ratchet. *Science* 2008;320:931–4.

[4] Morrow NR, Mason G. Recovery of oil by spontaneous imbibition. *Curr Opin Colloid Interface Sci* 2001;6:321–37.

[5] Singh H. A critical review of water uptake by shales. *J Nat Gas Sci Eng* 2016;34:751–66.

[6] Ho C-M, Tai Y-C. Micro-electro-mechanical-systems (MEMS) and fluid flows. *Ann Rev Fluid Mech* 1998;30:579–612.

[7] Gruener S, Sadjadi Z, Hermes HE, Kityk AV, Knorr K, Egelhaaf SU, et al. Anomalous front broadening during spontaneous imbibition in a matrix with elongated pores. *Proc Natl Acad Sci USA* 2012;109:10245–50.

[8] Gruener S, Huber P. Imbibition in mesoporous silica: rheological concepts and experiments on water and a liquid crystal. *J Phys Condens Matter* 2011;23:184109.

[9] Gruener S, Huber P. Spontaneous imbibition dynamics of an n -alkane in nanopores: evidence of meniscus freezing and monolayer sticking. *Phys Rev Lett* 2009;103:174501.

[10] Handy L. Determination of effective capillary pressures for porous media from imbibition data. *Trans AIME*. 1960;219:75–80.

[11] O'Loughlin M, Wilk K, Priest C, Ralston J, Popescu MN. Capillary rise dynamics of aqueous glycerol solutions in glass capillaries: a critical examination of the Washburn equation. *J Colloid Interface Sci* 2013;411:257–64.

[12] Dimitrov DI, Milchev A, Binder K. Capillary rise in nanopores: molecular dynamics evidence for the Lucas-Washburn equation. *Phys Rev Lett* 2007;99:054501.

[13] Cai J, Yu B. A discussion of the effect of tortuosity on the capillary imbibition in porous media. *Trans Porous Med* 2011;89:251–63.

[14] Cai JC, Perfect E, Cheng CL, Hu XY. Generalized modeling of spontaneous imbibition based on Hagen-Poiseuille flow in tortuous capillaries with variably shaped apertures. *Langmuir* 2014;30:5142–51.

[15] Reyssat M, Courbin L, Reyssat E, Stone HA. Imbibition in geometries with axial variations. *J Fluid Mech* 2008;615:335–44.

[16] Reyssat M, Sangne LY, van Nierop EA, Stone HA. Imbibition in layered systems of packed beads. *EPL* 2009;86.

[17] Yang L, Ge H, Shi X, Cheng Y, Zhang K, Chen H, et al. The effect of microstructure and rock mineralogy on water imbibition characteristics in tight reservoirs. *J Nat Gas Sci Eng* 2016.

[18] Hu Q, Ewing RP, Dultz S. Low pore connectivity in natural rock. *J Contam Hydrol* 2012;133:76–83.

[19] Hu QH, Liu XG, Gao ZY, Liu SG, Zhou W, Hu WX. Pore structure and tracer migration behavior of typical American and Chinese shales. *Pet Sci* 2015;12:651–63.

[20] Liu H-H, Lai B, Chen J. Unconventional spontaneous imbibition into shale matrix: theory and a methodology to determine relevant parameters. *Trans Porous Med* 2016;111:41–57.

[21] Bultreys T, De Boever W, Cnudde V. Imaging and image-based fluid transport modeling at the pore scale in geological materials: a practical introduction to the current state-of-the-art. *Earth Sci Rev* 2016;155:93–128.

[22] Kelly S, El-Sobky H, Torres-Verdin C, Balhoff MT. Assessing the utility of FIB-SEM images for shale digital rock physics. *Adv Water Resour* 2016;95:302–16.

[23] Wildenschild D, Sheppard AP. X-ray imaging and analysis techniques for quantifying pore-scale structure and processes in subsurface porous medium systems. *Adv Water Resour* 2013;51:217–46.

[24] Øren PE, Bakke S. Process based reconstruction of sandstones and prediction of transport properties. *Trans Porous Med*. 2002;46:311–43.

[25] Yeong C, Torquato S. Reconstructing random media. II. Three-dimensional media from two-dimensional cuts. *Phys Rev E* 1998;58:224–33.

[26] Ju Y, Zheng J, Epstein M, Sudak L, Wang J, Zhao X. 3D numerical reconstruction of well-connected porous structure of rock using fractal algorithms. *Comput Method Appl M* 2014;279:212–26.

[27] Wang M, Pan N. Predictions of effective physical properties of complex multi-phase materials. *Mater Sci Eng R Rep* 2008;63:1–30.

[28] Wang M, Wang J, Pan N, Chen S. Mesoscopic predictions of the effective thermal conductivity for microscale random porous media. *Phys Rev E* 2007;75:036702.

[29] Falcucci G, Ubertini S, Biscarini C, Francesco SD, Chiappini D, Palpacelli S. Lattice Boltzmann methods for multiphase flow simulations across scales. *Commun Comput Phys* 2011;9:269–96.

[30] Tölke J, Freudiger S, Krafczyk M. An adaptive scheme using hierarchical grids for lattice Boltzmann multi-phase flow simulations. *Comput Fluids*. 2006;35:820–30.

[31] Sun Y, Kharaghani A, Tsotsas E. Micro-model experiments and pore network simulations of liquid imbibition in porous media. *Chem Eng Sci* 2016;150:41–53.

[32] Huang X, Bandilla KW, Celia MA. Multi-physics pore-network modeling of two-phase shale matrix flows. *Trans Porous Med* 2015;111:1–19.

[33] Chen S, Gary DD. Lattice Boltzmann method for fluid flows. *Ann Rev Fluid Mech* 1998;30:329–64.

[34] Yuan P, Schaefer L. Equations of state in a lattice Boltzmann model. *Phys Fluids* 2006;18:042101.

[35] Kupershtokh AL, Medvedev DA, Karpov DI. On equations of state in a lattice Boltzmann method. *Comput Math Appl* 2009;58:965–74.

- [36] Xu A, Zhao TS, An L, Shi L. A three-dimensional pseudo-potential-based lattice Boltzmann model for multiphase flows with large density ratio and variable surface tension. *Int J Heat Fluid Flow*. 2015;56:261–71.
- [37] Li Q, Luo KH. Achieving tunable surface tension in the pseudopotential lattice Boltzmann modeling of multiphase flows. *Phys Rev E*. 2013;88:053307.
- [38] Ahrenholz B, Tölke J, Lehmann P, Peters A, Kaestner A, Krafczyk M, et al. Prediction of capillary hysteresis in a porous material using lattice-Boltzmann methods and comparison to experimental data and a morphological pore network model. *Adv Water Resour* 2008;31:1151–73.
- [39] Genty A, Pot V. Numerical simulation of 3D liquid–gas distribution in porous media by a two-phase TRT Lattice Boltzmann method. *Transp Porous Med* 2013;96:271–94.
- [40] Hyvälouma J, Raiskinmäki P, Jäsberg A, Koponen A, Kataja M, Timonen J. Simulation of liquid penetration in paper. *Phys Rev E* 2006;73:036705.
- [41] Pan C, Hilpert M, Miller CT. Lattice-Boltzmann simulation of two-phase flow in porous media. *Water Resour Res* 2004;40:62–74.
- [42] Ammar S, Pernaudat G, Trépanier J-Y. A multiphase three-dimensional multi-relaxation time (MRT) lattice Boltzmann model with surface tension adjustment. *J Comput Phys* 2017;343:73–91.
- [43] Liu H, Kang Q, Leonardi CR, Schmieschek S, Narváez A, Jones BD, et al. Multiphase lattice Boltzmann simulations for porous media applications. *Comput Geosci* 2016;20:777–805.
- [44] Sukop MC, Huang H, Lin CL, Deo MD, Oh K, Miller JD. Distribution of multiphase fluids in porous media: comparison between lattice Boltzmann modeling and micro-x-ray tomography. *Phys Rev E* 2008;77:026710.
- [45] Ahrenholz B, Niessner J, Helmig R, Krafczyk M. Pore-scale determination of parameters for macroscale modeling of evaporation processes in porous media. *Water Resour Res* 2011;47 n/a-n/a.
- [46] Gunstensen AK, Rothman DH, Zaleski S, Zanetti G. Lattice Boltzmann model of immiscible fluids. *Phys Rev A* 1991;43:4320.
- [47] Fakhari A, Geier M, Lee T. A mass-conserving lattice Boltzmann method with dynamic grid refinement for immiscible two-phase flows. *J Comput Phys* 2016;315:434–57.
- [48] Shan X, Chen H. Lattice Boltzmann model for simulating flows with multiple phases and components. *Phys Rev E* 1993;47:1815–19.
- [49] Shan X, Chen H. Simulation of nonideal gases and liquid-gas phase transitions by the lattice Boltzmann equation. *Phys Rev E* 1994;49:2941.
- [50] Swift MR, Orlandini E, Osborn WR, Yeomans JM. Lattice Boltzmann simulations of liquid-gas and binary fluid systems. *Phys Rev E* 1996;54:5041–52.
- [51] Xie C, Zhang J, Bertola V, Wang M. Droplet evaporation on a horizontal substrate under gravity field by mesoscopic modeling. *J Colloid Interface Sci* 2016;463:317–23.
- [52] He X, Chen S, Zhang R. A Lattice Boltzmann scheme for incompressible multiphase flow and its application in simulation of Rayleigh–Taylor instability. *J Comput Phys* 1999;152:642–63.
- [53] I Chen, Q Kang, Mu Y, He YL, Tao WQ. A critical review of the pseudopotential multiphase lattice Boltzmann model: methods and applications. *Int J Heat Mass Transfer* 2014;76:210–36.
- [54] Li Q, Luo KH, Kang QJ, He YL, Chen Q, Liu Q. Lattice Boltzmann methods for multiphase flow and phase-change heat transfer. *Prog Energy Combust Sci* 2016;52:62–105.
- [55] Huang H, Sukop MC, Lu XY. Multiphase lattice Boltzmann methods: theory and application. Wiley-Blackwell; 2015.
- [56] Sukop MC, Thorne DTJ. Lattice Boltzmann modeling: an introduction for geoscientists and engineers. New York: Springer; 2006.
- [57] Raiskinmäki P, Shakib-Manesh A, Jäsberg A, Koponen A, Merikoski J, Timonen J. Lattice-Boltzmann simulation of capillary rise dynamics. *J Stat Phys* 2002;107:143–58.
- [58] Diotallevi F, Biferale L, Chibbaro S, Lamura A, Pontrelli G, Sbragaglia M, et al. Capillary filling using lattice Boltzmann equations: the case of multiphase flows. *Eur Phys J Spec Top* 2009;166:111–16.
- [59] Diotallevi F, Biferale L, Chibbaro S, Pontrelli G, Toschi F, Succi S. Lattice Boltzmann simulations of capillary filling: finite vapour density effects. *Eur Phys J Spec Top* 2009;171:237–43.
- [60] Son S, Chen L, Kang Q, Derome D, Carmeliet J. Contact angle effects on pore and corner arc menisci in polygonal capillary tubes studied with the pseudopotential multiphase lattice Boltzmann model. *Computation* 2016:4.
- [61] De Maio A, Palpacelli S, Succi S. A new boundary condition for three-dimensional lattice Boltzmann simulations of capillary filling in rough microchannels. *Commun Comput Phys* 2011;9:1284–92.
- [62] Bhatnagar PL, Gross EP, Krook M. A model for collision processes in gases. I. Small amplitude processes in charged and neutral one-component systems. *Phys Rev* 1954;94:511–25.
- [63] Wang M, Pan N, Wang JK, Chen SY. Lattice Poisson–Boltzmann simulations of electroosmotic flows in charged anisotropic porous media. *Commun Comput Phys* 2007;2:1055–70.
- [64] Huang H, Thorne DT, Schaap MG, Sukop MC. Proposed approximation for contact angles in Shan-and-Chen-type multicomponent multiphase lattice Boltzmann models. *Phys Rev E* 2007;76:75–80.
- [65] Feng YT, Han K, Owen DRJ. Coupled lattice Boltzmann method and discrete element modelling of particle transport in turbulent fluid flows: computational issues. *Int J Numer Method Eng* 2007;72:1111–34.
- [66] Benzi R, Biferale L, Sbragaglia M, Succi S, Toschi F. Mesoscopic modeling of a two-phase flow in the presence of boundaries: the contact angle. *Phys Rev E* 2006;74:021509.
- [67] Li Q, Luo KH, Kang QJ, Chen Q. Contact angles in the pseudopotential lattice Boltzmann modeling of wetting. *Phys Rev E* 2014;90:053301.
- [68] Huang H, Krafczyk M, Lu X. Forcing term in single-phase and Shan-Chen-type multiphase lattice Boltzmann models. *Phys Rev E* 2011;84:046710.
- [69] Li Q, Luo KH, Li XJ. Lattice Boltzmann modeling of multiphase flows at large density ratio with an improved pseudopotential model. *Phys Rev E* 2013;87:053301.
- [70] Wolf FG, dos Santos LOE, Philippi PC. Micro-hydrodynamics of immiscible displacement inside two-dimensional porous media. *Microfluid Nanofluid* 2008;4:307–19.
- [71] Siliu D, Patzek T. Pore space morphology analysis using maximal inscribed spheres. *Phys A Stat Mech Appl* 2006;371:336–60.
- [72] Connington K, Lee T. A review of spurious currents in the lattice Boltzmann method for multiphase flows. *J Mech Sci Technol* 2012;26:3857.
- [73] Sbragaglia M, Benzi R, Biferale L, Succi S, Sugiyama K, Toschi F. Generalized lattice Boltzmann method with multirange pseudopotential. *Phys Rev E* 2007;75:95–105.